/

NASA TECHNICAL MEMORANDUM 108999

p. 43

AN ANALYSIS OF FIBER-MATRIX INTERFACE FAILURE STRESSES FOR A RANGE OF PLY STRESS STATES

J. H. CREWS, R. A. NAIK, AND
S. J. LUBOWINSKI

JULY 1993

(NASA-TM-108999) AN ANALYSIS OF
FIBER-MATRIX INTERFACE FAILURE
STRESSES FOR A RANGE OF PLY STRESS
STATES (NASA) 43 p

N94-11276

Unclas

G3/24 0177081

National Aeronautics and
Space Administration
Langley Research Center
Hampton, Virginia 23681-0001

ABSTRACT

A graphite/bismaleimide laminate was prepared without the usual fiber treatment and was tested over a wide range of stress states to measure its ply cracking strength. These tests were conducted using off-axis flexure specimens and produced fiber-matrix interface failure data over a correspondingly wide range of interface stress states. The absence of fiber treatment weakened the fiber-matrix interfaces and allowed these tests to be conducted at load levels that did not yield the matrix. An elastic micromechanics computer code was used to calculate the fiber-matrix interface stresses at failure. Two different fiber-array models (square and diamond) were used in these calculations to analyze the effects of fiber arrangement as well as stress state on the critical interface stresses at failure. This study showed that both fiber-array models were needed to analyze interface stresses over the range of stress states. A linear equation provided a close fit to these critical stress combinations and, thereby, provided a fiber-matrix interface failure criterion. These results suggest that prediction procedures for laminate ply cracking can be based on micromechanics stress analyses and appropriate fiber-matrix interface failure criteria. However, typical structural laminates may require elastoplastic stress analysis procedures that account for matrix yielding, especially for shear-dominated ply stress states.

Keywords.- composite, fiber-matrix interface, stress analysis, ply strength, test, off-axis flexure.

INTRODUCTION

Ply cracks are usually the first damage that develops when a laminate begins to fail under either static or cyclic tensile loading. These ply cracks probably start as fiber-matrix interface microcracks which coalesce into macrocracks. Studies of fiber-matrix interface failures could, therefore, provide important insight regarding ply cracking. Unfortunately, however, most interface studies have focused on single-fiber tests [1,2,3]. These tests cannot account for fiber-to-fiber interactions which elevate the interface stresses. Also, single-fiber tests do not involve interface stress states typical of ply cracking conditions in structures. Single-fiber loading produces shear-dominated stress states, involving interface normal stresses which are often compressive. In contrast, adhesion analyses show that interface failures usually occur under tension-dominated stress states [4]. The objective of the present study was to analyze fiber-matrix interface stresses at ply failure for a range of stress states and then to develop a fiber-matrix interface failure criterion.

Ply cracking tests were conducted using specimens with a weakened fiber-matrix interface. These unidirectional specimens were cut with various "off-axis" fiber orientations from a 24-ply, graphite/bismalimide laminate (G40-800/5250-2), fabricated without the usual oxidative fiber treatment. The specimens were failed under three-point loading, applied using an off-axis flexure apparatus introduced in reference 5. This apparatus allowed testing over a wide range of ply stress states.

For analysis purposes, the composite was assumed to consist of a uniform array of fibers and to be free of defects. Also, the onset of ply cracking was assumed to correspond to the onset of microcracking at the fiber-matrix interface. These assumptions allowed the critical fiber-matrix interface stresses associated with ply cracking to be calculated using a unit-cell micromechanics approach. The micromechanics computer code MICSTRAN [5] provided these interface stresses. Fiber-to-fiber interactions were investigated by using two different fiber-array models (square and diamond) in these calculations.

Test results were first presented as ply cracking strength for a range of multiaxial stress states. Photomicrographs of fracture surfaces were examined to establish the existence of interface failures. The computed interface stresses at failure were then compared for the range of test cases, using the two fiber-array models to determine the critical interface stress conditions. An interface failure criterion was established by fitting an equation to these critical stress conditions. Finally, these results were discussed and additional research topics were recommended.

NOMENCLATURE

b	specimen width
d	specimen thickness
L	distance between specimen supports
P	applied load
P_f	failure load
r,θ,z	unit cell coordinates
w	z-direction displacement
x,y,z	laminate coordinates
x_1,x_2,x_3	ply coordinates
x_f	x-axis distance to fracture surface
α	specimen fiber angle
σ_{11}	ply normal stress in fiber direction
τ_{12}	ply shear stress in fiber direction
σ_{22}	ply normal stress perpendicular to fibers
σ_{xb}	beam theory bending stress
$\sigma_{xx},\tau_{xy},\sigma_{yy}$	laminate stresses
$\sigma_{rr},\tau_{r\theta},\tau_{rz}$	fiber-matrix interface stresses
$\tau_{\theta z},\sigma_{\theta\theta},\sigma_{zz}$	matrix stresses

TEST PROCEDURE

The present study involved testing off-axis specimens in bending to produce ply cracking failures under multiaxial stress states. The off-axis flexure (OAF) test apparatus was developed in reference 5 to exploit the simplicity of the off-axis specimen while avoiding the problems associated with gripping this specimen [7,8]. The OAF test specimen and apparatus are discussed in detail in reference 5 and are only briefly described here.

Specimen Configuration and Loading

Figure 1(a) shows the plan view of the OAF specimen. Specimens were cut from 24-ply unidirectional laminates made with G40-800/5250-2 graphite/bismaleimide. Each specimen orientation was indicated by the fiber angle α, as shown in figure 1(a). The fiber angles of 90^o, 75^o, 60^o, 45^o, 30^o, and 15^o were used. Figure 1(b) shows the edge view of the specimen and the applied load (P). The 24-ply specimens used in this study had an average thickness (d) of 0.1080 in. Specimen width (b) was 0.213 in. and its length (L) was 2.10 in. As mentioned, these OAF specimens were prepared from a laminate that did not have the usual oxidative fiber treatment. For comparison, however, additional specimens were tested from a laminate which had the standard fiber treatment for this graphite/bismaleimide composite. All specimens were tested in a dry condition.

For the three-point loading shown in figure 1(b), the tensile bending stress σ_{xx} is largest on the lower surface at the midspan of the specimen. This uniaxial σ_{xx} can be resolved into the ply coordinate system (x_1,x_2,x_3)

as three multiaxial components: σ_{11}, τ_{12}, and σ_{22}. However, because fracture develops along the fiber-direction plane, the fiber-direction stress σ_{11} does not contribute to failure. As a result, the ply-level stress state that produces cracking consists only of τ_{12}, the longitudinal shear stress in the fiber direction and σ_{22}, the normal stress transverse to the fibers. By varying the fiber angle α, ply cracking failures can be studied for a range of τ_{12}- σ_{22} stress states.

Off-Axis Flexure Test

Because of its anisotropy, the off-axis specimen develops twist as well as flexure, as it deforms under the applied three-point bending loads. Figure 2(a) schematically illustrates this deformation with twist at each end of the specimen. The OAF test concept is illustrated in figure 2(b). The specimen supports are attached to ball bearings that rotate freely to accommodate twist without introducing a torque reaction. The loading nose prevents rotation at the specimen midspan and, thereby, stabilizes the specimen. The twist is, therefore, equal and opposite at the two specimen supports. This approach allows an off-axis specimen to be loaded to failure under bending stresses which can be simply calculated.

A photograph of the off-axis flexure apparatus is shown in figure 3. A one-piece steel base holds both ball bearings which were installed with a press fit. The specimen rests on steel supports (not visible in this photograph) having a 0.125 in. radius. These supports are bonded to spacers which are bonded to the inner race of each bearing. The steel loading nose also has a 0.125 in. radius. This three-point bending apparatus has a 1.60 in. span (L), which allowed the specimen to overhang each support by 0.25

in. Specimens were loaded to failure using a screw-driven test machine with a displacement rate of 0.02 in/min.

An end-view photograph of the apparatus is shown in figure 4. This figure shows the specimen supports and the spacers that center the specimen cross-section on the axis of rotation for the two ball bearings. The specimen twist is evidenced by the opposite rotations of these supports. The end of this 15° specimen, which is loaded to about 80% of its failure load, was painted gray to make its twist more visible.

A 3D finite element analysis was conducted in reference 5 to compute stressed in the OAF specimen and then to evaluate the use of simple beam theory to calculate the specimen failure stresses. This stress analysis focused on the bottom surface of the specimen at its midspan, the expected failure initiation site. To facilitate comparisons, the finite element stresses were normalized by the maximum beam theory stress, σ_{xb}, calculated using

$$\sigma_{xb} = 3PL / 2bd^2 \qquad (1)$$

Results for the $\alpha = 45^\circ$ case are shown in figure 5 as computed stress distributions across the specimen width at its midspan (x=0). The symbols in this figure represent finite element results and the solid curves are fits to these results. Horizontal lines indicate the reference levels of 0 and 1 on the normalized stress scale. A uniform nodal displacement imposed at the specimen midspan produced the "applied" σ_{zz} stresses. This σ_{zz} distribution is nonuniform because of anticlastic curvature of the specimen at its midspan. The σ_{xx} bending stresses (solid circular symbols) are nearly uniform across the lower surface of the specimen. The σ_{yy} and τ_{xy} stresses (triangle and square symbols, respectively) at the bottom of the specimen are negligibly small. Because the σ_{xx} average across the width and the beam theory value differ only by about two percent, failure of this 45^{o} off-axis flexure specimen can be analyzed using beam theory with negligibly small errors.

Similar close agreement with beam theory was shown in reference 5 for the other off-axis angles. As a result, the test data can be analyzed using simple beam theory. For each test, the σ_{xb} can be computed using the measured failure load P_f in equation (1). The corresponding τ_{12} and σ_{22} stresses on the failure plane can then be calculated using

$$\tau_{12} = \sigma_{xb} \sin(\alpha) \cos(\alpha) \tag{2}$$

and

$$\sigma_{22} = \sigma_{xb} \sin^2(\alpha) \tag{3}$$

TEST RESULTS

Throughout each OAF test, the applied load and the loading-nose displacement were recorded. Typical load to failure test results are shown in figures 6(a) and 6(b) for the untreated and standard laminates, respectively. Comparison of these figures shows that the untreated laminate failed at about one-half the load required for the standard laminate. Comparison of tables 1 and 2 shows a similar result. Because these two laminates were identical except for their fiber treatments, these strength differences were believed to be caused by different levels of fiber-matrix adhesion strength. In all tests, the specimens failed abruptly without any detected indication of damage accumulation or stable crack growth. These results support the previously discussed assumption that the observed ply cracking coincided with the onset of fiber-matrix interface microcracking and the corresponding assumption that this ply cracking was governed by the fiber-matrix interface stresses.

For the untreated laminate, the load-displacement curves in figure 6(a) are linear to failure for all six fiber angles. In contrast, for the standard laminate, the curves in figures 6(b) are noticeably nonlinear for $\alpha = 15^{\circ}$, 30°, and 45°. To emphasize this nonlinearity, dashed lines are drawn as projections of the linear response. This nonlinearity was believed to be caused by matrix yielding that preceded specimen failure. Unfortunately, the simple beam theory analysis of the present study could not account for this nonlinear response. As a result, the present study focused on the untreated laminate. Although, this untreated laminate was not viewed as a viable structural material, it provided a useful set of failure data for a wide range of stress states without the complications of matrix yielding. An analysis of these data provided some insight regarding the effects of stress state on fiber-matrix interface failures that should be relevant to other laminates.

The test data for the untreated laminate were first analyzed to study the possibility that all failures initiated at the specimen edges, in which case the test results could be influenced by edge effects. This possibility was investigated because stress singularities probably exist where the fiber-matrix interfaces intersect the free edges of a loaded OAF specimen [9]. The location of the fracture surface relative to the specimen midspan provided some insight about the probable failure initiation site. For each test, the distance (x_f) along the x-axis to the fracture surface was measured using a machinist scale (see table 1).

If all failures were to start at one of the specimen edges at its midspan, then all x_f values would equal either $b/2\tan\alpha$ or $-b/2\tan\alpha$. To explore this extreme case, figure 7 shows the measured x_f values plotted against the computed $b/\tan\alpha$ values for the six different fiber angles. The two diagonal lines in this figure correspond to x_f equal to $b/2\tan\alpha$ and $-b/2\tan\alpha$. Clearly the scattered data do not conform to this extreme case of all failures being edge failures starting at the specimen midspan. More realistically, however, edge failure initiation sites would be distributed about the midspan location. The corresponding x_f data would be distributed about either $b/2\tan\alpha$ or $-b/2\tan\alpha$ for each α case. These distributions would cause 50% of the x_f values to lie between the two diagonal lines in figure 7. In contrast, about 87% of the data lie between these lines, suggesting that most failures started away from the specimen edges. As a result, the OAF test data were considered to represent ply cracking strength and were not believed to be seriously influenced by specimen edge effects.

The multiaxial ply stresses σ_{22} and τ_{12} on the failure plane were computed for each specimen failure load, using equations (2) and (3). These results are presented in figure 8. Each symbol represents an average of six tests from table 1 and the tick marks indicate the data range for each test case. The range of stress states in this figure is typical of conditions that produce ply cracking in laminated composite structures [5]. The solid curve provides a good fit (second order polynomial) to these ply strength data. This solid curve was used to represent the ply strength in the subsequent analyses to eliminate the effects of ply data scatter on the interface stress calculations.

Figure 9 shows photomicrographs of typical fracture surfaces. For all three cases in this figure, the 5.0 μm graphite fibers are clearly visible. The smooth fiber surfaces in this figure support the assumption of a fiber-matrix interface failure mode for this laminate.

FIBER-MATRIX INTERFACE STRESSES

MICSTRAN Computer Code

The MICSTRAN computer program [6] was used to calculate stresses at the fiber-matrix interface. This micromechanics program provides an elastic analysis of constituent stresses, using a stress-function approach with a unit-cell representation of the composite. MICSTRAN can compute the composite constituent stresses corresponding to each of the ply stress components as well as thermal stresses due to a temperature change. The constituent properties used in this study are shown in table 3.

The random arrangement of fibers within a ply has often been approximated using either a square, diamond, or hexagonal array. However, all of these arrays probably occur at various locations within a ply. Because these arrays produce different stress concentrations under different types of loading, micromechanics failure analyses should consider various arrays, and failure predictions should be based on the most severe array for a given loading case. Because the square and diamond arrays produce higher stress concentrations than the hexagonal array [10,11], MICSTRAN allows analyses by both of these two arrays. The square and diamond arrays used with MICSTRAN are shown in figure 10.

Thermal and Mechanical Loading

To illustrate the individual effects of thermal and mechanical loading, results are presented first for thermal cooldown from the cure temperature, then for transverse tension loading (σ_{22}), and finally for longitudinal shear loading (τ_{12}). For each case, matrix stresses along the fiber-matrix interface were computed in the fiber-coordinate system (r, θ, z) using both the square and diamond unit-cell arrays. Because of symmetry, stresses needed to be computed only for θ between 0 and 90°.

Figure 11(a) shows these stresses for a square array model subjected to a temperature change of -280°F, corresponding to cooldown from the 350°F cure temperature to 70°F room temperature. Only four stress components are shown in figure 11(a) because $\tau_{\theta z}$ and τ_{rz} are zero. Although the $\sigma_{\theta\theta}$ and σ_{zz} stresses are larger than the others, they are matrix stresses that act parallel to the interface and, therefore, do not contribute directly to interface failure. These two stress components will not be used in the subsequent failure analysis and are shown here for completeness. In contrast, σ_{rr} and $\tau_{r\theta}$ act on the interface and can influence its failure. These two thermal stresses will be superimposed with stresses due to mechanical loading. Notice that σ_{rr} in figure 11(a) has its largest compressive value at $\theta=0^{\circ}$. Figure 11(b) shows thermal stresses for the diamond array model. For this case, σ_{rr} is tensile near $\theta=0$. This difference in σ_{rr} signs for the two arrays will be discussed later.

Matrix stresses along the interface for σ_{22} loading are shown in figures 12(a) and 12(b) for the square and diamond arrays, respectively. The σ_{22} level of 5.0 ksi was used because it is typical of ply strengths shown earlier in figure 8. The τ_{rz} and $\tau_{\theta z}$ for σ_{22} loading are again zero. The largest stress in both figures 12(a) and 12(b) is σ_{rr} which has a tensile peak at $\theta=0$. Notice that the σ_{rr} peak value is about 50% higher for the square array analysis. The $\tau_{r\theta}$ curves peak near $\theta=45^{\circ}$, and the diamond-array curve is about 20% higher than the square array curve.

Figures 13(a) and 13(b) show the non-zero stresses along the interface for loading produced by $\tau_{12}=5.0$ ksi. The τ_{rz} curve for the square array has its peak value at $\theta=0$ and is more than 30% higher than the diamond array peak at $\theta=45^{\circ}$.

Comparison of figures 11, 12, and 13 shows that, in general, the interface stresses σ_{rr}, $\tau_{r\theta}$, and τ_{rz} have different signs, peak values, and peak locations for the different types of loading and analysis arrays. As a result, the critical combinations of interface stresses corresponding to failure cannot be determined simply by inspection.

Failure Stresses for Combined Thermal and Mechanical Loading

The fiber-matrix interface stresses for a typical case of combined thermal and mechanical loading are shown in figure 14. These results were computed using a temperature change of -280°F and ply stresses $\sigma_{22}=\sigma_{12}=4.46$ ksi as input for MICSTRAN. Because this input corresponds to the failure conditions for the $\alpha=45^{\circ}$ OAF test, the results in either figure 14(a) or 14(b) should represent a critical combination of stresses somewhere along the fiber-matrix interface. However, this critical location is not obvious. Also, it is not obvious which is the more critical of the two cases.

To simplify this analysis of critical interface conditions, the $\tau_{r\theta}$ and τ_{rz} interface shear stresses were combined into an effective shear stress τ_{eff} using

$$\tau_{eff} = (\tau_{r\theta}^2 + \tau_{rz}^2)^{1/2} \qquad (4)$$

This approach reduced the analysis of critical interface conditions to the study of the combined effects of σ_{rr} and τ_{eff}.

An interface "failure curve" was established in terms of σ_{rr} and τ_{eff}. This failure curve was assumed to be an upper envelope for all the various computed combinations of interface stress, corresponding to specimen failure with the different fiber orientations. Therefore, any σ_{rr}- τ_{eff} combinations that lie on this curve would corresponded to critical interface conditions at failure. To introduce the procedure used to establish this curve, computed $\sigma_{rr}$and τ_{eff} values are first shown in figure 15 for 5^o intervals along the interface for the α=45^o test case. Again, because these interface stresses correspond to failure, one of the σ_{rr}-τ_{eff} combinations in either figure 15(a) or 15(b) was assumed to initiate the interface failure. This critical interface stress combination is not immediately identifiable in figure 15; but once it is determined, it establishes one point on the failure curve. In general, each OAF test case produced a different interface stress state and thereby defines a different point on this curve. When all of the six OAF cases are plotted together, the six critical interface σ_{rr}-τ_{eff} combinations can be identified and the interface failure curve can be established.

Because each of the six OAF test cases was analyzed using both the square and diamond array models, this procedure involves a total of twelve sets of results to be analyzed. To simplify the procedure and to compare the two models, their results are first presented separately, as shown in figure 16. Figure 16(a) shows the α=45^ocase replotted from figure 15(a) together with curves for the other five α cases, computed using the square array. The point where each curve was estimated to be tangent to an upper envelope is indicated by a solid symbol. Figure 16(b) shows similar results for the diamond array, with two points selected for the 15° curve.

A curve was fitted to the solid symbols in figure 16(a) and a similar curve was fitted for figure 16(b). These two "candidate failure curves" are compared in figure 17(a). For the σ_{rr}-dominated stress states ($\alpha=45^{\circ}$- 90°), the diamond-array curve lies above the square-array curve. Therefore, the diamond-array stresses are more severe than the square-array results in this stress state range. However, in the τ_{eff}-dominated range ($\alpha=15^{\circ}$- 30°), the square array results are more severe.

The relatively high severity of the diamond array solution for the $\sigma_{\theta\theta}$ dominated stress states in figure 17(a) can be explained by thermal stresses shown earlier. Figure 11(b) showed that the thermal σ_{rr} for the diamond array is tensile at $\theta=0^{\circ}$. This tensile σ_{rr} adds to the tensile σ_{rr} produced by σ_{22} loading (see figure 12(b)) to create a critical interface condition at $r=0^{\circ}$. In contrast, for the square array, figure 11(a) showed that thermal cooldown produces large compressive σ_{rr} values near $\theta=0^{\circ}$, which tend to cancel the tensile σ_{rr} caused by σ_{22} loading. As a result, the peak σ_{rr} conditions are lower for the square array.

Finally, to establish the interface failure envelope for the untreated laminate, the solid symbols in figure 17(a) were replotted in figure 17(b) and fitted with an equation. Figure 17(b) shows that a linear fit is a reasonably good representation of these critical interface stresses. This curve can be viewed as the failure criterion for the fiber-matrix interface. Consequently, this curve could be used together with MICSTRAN to predict ply cracking in the untreated laminate for various layups, configurations, and loadings.

This analysis of the untreated laminate shows that thermal stresses had a significant effect on the results. However, for laminates with stronger fiber-matrix interfaces, the thermal stresses should have less relative importance. But for thermoplastic laminates, the thermal stresses will be larger than in the present study and could have more influence. In general, the effects of both thermal and mechanical loading need to be considered and, as illustrated by figure 17(b), both the diamond and square array models should be used to calculate the critical interface conditions.

Future research in this area should focus on elastoplastic stress analyses at the ply level as well as the fiber-matrix level. Likely laminate sites for ply cracking should be analyzed to determine the relative criticality of the shear stress dominated plies and the transverse tension dominated plies, for typical layups and loadings. Matrix yielding could reduce the criticality of the shear dominated plies and may simultaneously increase criticality of the tension dominated plies. Despite yielding in the shear dominated plies, the tensile dominated plies may crack first, perhaps before they yield. In this case, the elastic MICSTRAN code can provide the computational basis for predicting the onset of such ply cracking. In the more likely general case, however, elastoplastic micromechanics stress analyses will be required to make such predictions.

CONCLUDING REMARKS

A graphite/bismaleimide (G40-800/5250-2) laminate was prepared without the usual fiber treatment and was tested to produce fiber-matrix interface failures over a range of stress states. These tests were conducted using off-axis flexure specimens having a 24-ply unidirectional layup. Next, the fiber-matrix interface stresses corresponding to specimen failure were calculated using a micromechanics computer code. These stresses were then analyzed to develop a fiber-matrix interface failure criteria for a range of stress states.

The off-axis flexure test provided ply cracking data for the desired wide range of stress states. Photomicrographs of the fracture surface showed smooth fiber surfaces, supporting the assumption of fiber-matrix interface failures. The load-displacement curves were found to be linear, thereby allowing an elastic analysis of the fiber-matrix interface stresses at failure. In contrast, tests with a laminate having the standard fiber treatment produced nonlinear displacements for the shear dominated stress states. This nonlinearity was attributed to matrix yielding that preceded the fiber-matrix interface failures.

The MICSTRAN analysis of the untreated laminate was conducted using two micromechanics models: a square array of fibers and a diamond array. The diamond array produced higher fiber-matrix interface stresses for ply stress states dominated by transverse tension. But the square array produced higher interface stresses for shear dominated stress states. As a result, both micromechanics models were needed to analyze the full range of ply stress states at failure.

A linear equation provided a close fit to the critical interface stresses computed at failure. This close fit demonstrated that fiber-matrix interface strength correlated well with the measured ply strengths over the wide range of stress states tested. The failure criterion represented by this linear equation, therefore, provides a basis for predicting the onset of cracking in the untreated laminate for various layups, configurations, and loadings. For this untreated laminate, such predictions could be made using elastic micromechanics procedures. For most laminates, however, the micromechanics procedures will probably need to account for matrix yielding that develops before ply cracking, especially for the shear-dominated stress states.

REFERENCES

1. Narkis, M., Chen, J. H., and Pipes, R. B.: "Review of Methods for Characterization of Interfacial Fiber-Matrix Interaction", Polymer Composites, Vol. 9, No. 4, August 1988, pp. 245-251.
2. Strong, K. L.: "Interfaces of Organic Matrices and Graphite Fiber Composites", Wright Research Development Center, Wright-Patterson Air Force Base, WRDC- TR-89-4063, July 1989.
3. Herrera-Franco, P. J. and Drzal, L. T.: "Comparison of Methods for the Measurement of Fiber/Matrix Adhesion in Composites", Composites, Vol. 23, No. 1, January, 1992, pp. 2-27.
4. Adams, R. D. and Wake, W. C.: Structural Adhesive Joints in Engineering, Elsevier Applied Science Publishers Ltd, 1984, p16.
5. Crews, John H., Jr. and Naik, R. A.: "Measurement of Multiaxial Ply Strength by an Off-Axis Flexure Test," NASA TM 107570, March 1992.
6. Naik, R. A.: "Micromechanical Combined Stress Analysis - MICSTRAN, a Users Manual," NASA CR 189694, October 1992, (Also available as NASA LAR-15005, COSMIC, 1992)
7. Rizzo, R. R.: "More on the Influence of End Constraints on Off-Axis Tensile Tests", J Composite Materials, Vol. 3, April 1969, pp. 202-219.
8. Sun, C. T. and Berreth, S. P.: "A New End Tab Design for Off-Axis Tension Test of Composite Materials", Journal of Composite Materials, Vol. 22, August 1988, pp. 766-779.

9. Raju, I. S. and Crews, J. H., Jr.: "Interlaminar Stress Singularities at a Straight Free Edge in Composite Laminates," Computers and Structures, Vol. 14, No. 1-2, 1981, pp. 21-28.

10. Foye, R. L.: "An Evaluation of Various Engineering Estimates of the Transverse Properties of Unidirectional Composites," Proc. 10th Nat. Symp., Soc. Aerosp. Mater. Process Eng., San Diego, CA, Nov. 9-11, 1966, pp. 152-164.

11. Naik, R. A. and Crews, J. H., Jr.: "Closed-Form Analysis of Fiber-Matrix Interface Stresses under Thermo-Mechanical Loading," NASA TM 107575, March 1992.

12. BASF 5250-2 Prepreg Properties, BASF Structural Materials, Inc., April 1987.

13. Celion Carbon Fibers Material Properties: G40-800, BASF Structural Materials, Inc., February, 1990.

14. Adams, D. F. and Schaffer, B. G.: "Analytical/Experimental Correlations of Stiffness Properties of Unidirectional Composites," Composites Technology Review, Vol.4, No.2, Summer 1982, pp 45-48.

15. Zimmerman, R. S. and Adams, D. F.: "Mechanical Properties of Neat Polymer Matrix Materials and Their Unidirectional Carbon Fiber-Reinforced Composites," NASA CR 181631, December 1988.

Table 1. Test results for untreated laminate.

α (deg)	b (in.)	d (in.)	x_f (in.)	P_f (lb)
90	0.2158	0.1046	0.05	5.028
	0.2161	0.1049	-0.04	5.238
	0.2163	0.1052	0.00	5.213
	0.2097	0.1095	-0.01	5.458
	0.2120	0.1106	0.02	6.252
	0.2124	0.1107	0.00	6.000
75	0.2151	0.1093	-0.01	7.157
	0.2148	0.1080	0.06	6.483
	0.2146	0.1099	-0.02	6.615
	0.2149	0.1073	0.01	6.059
	0.2144	0.1097	0.00	6.937
	0.2149	0.1067	-0.03	5.294
60	0.2152	0.1070	0.00	6.121
	0.2149	0.1065	0.01	6.389
	0.2147	0.1080	0.02	7.305
	0.2128	0.1088	-0.01	7.020
	0.2124	0.1105	0.00	7.718
	0.2128	0.1080	-0.06	7.356
45	0.2146	0.1089	-0.12	9.213
	0.2146	0.1068	-0.10	8.252
	0.2142	0.1068	-0.04	9.868
	0.2138	0.1070	0.07	8.405
	0.2136	0.1083	0.02	7.807
	0.2137	0.1070	-0.02	8.867
30	0.2141	0.1098	0.17	15.38
	0.2137	0.1083	-0.09	15.36
	0.2141	0.1074	0.19	14.87
	0.2137	0.1075	0.04	15.27
	0.2131	0.1095	-0.16	17.09
	0.2135	0.1092	-0.14	15.66
15	0.2129	0.1105	-0.10	35.06
	0.2142	0.1101	0.35	35.73
	0.2139	0.1100	-0.20	35.29
	0.2129	0.1056	0.30	28.08
	0.2127	0.1071	-0.26	28.97
	0.2130	0.1055	-0.31	32.82

Table 2. Test results for the standard laminate.

α (deg)	b (in.)	d (in.)	x_f (in.)	P_f (lb)
90	0.2124	0.1032	0.05	14.67
	0.2128	0.1032	-0.04	11.71
	0.2124	0.1041	-0.06	13.55
	0.2139	0.1089	0.02	12.34
	0.2142	0.1084	-0.01	12.75
	0.2144	0.1079	-0.03	13.08
75	0.2130	0.1068	0.03	14.25
	0.2075	0.1058	0.01	12.63
	0.2127	0.1074	0.02	15.15
	0.2146	0.1074	0.05	12.17
	0.2147	0.1056	0.00	12.54
	0.2146	0.1066	-0.03	13.34
60	0.2139	0.1054	-0.11	16.87
	0.2106	0.1049	0.04	14.75
	0.2146	0.1062	-0.04	16.23
	0.2145	0.1090	-0.02	15.19
	0.2150	0.1075	0.02	16.85
	0.2140	0.1088	0.14	16.32
45	0.2129	0.1056	0.02	22.44
	0.2130	0.1053	-0.13	18.92
	0.2128	0.1057	0.09	20.89
	0.2149	0.1057	0.03	20.85
	0.2152	0.1066	0.09	19.17
	0.2148	0.1067	-0.01	19.60
30	0.2127	0.1054	-0.21	33.53
	0.2124	0.1038	-0.15	34.85
	0.2127	0.1044	-0.17	33.15
	0.2148	0.1075	-0.11	32.16
	0.2143	0.1080	-0.01	33.54
	0.2145	0.1080	-0.22	35.14
15	0.2135	0.1068	0.30	80.00
	0.2110	0.1048	-0.28	76.51
	0.2131	0.1051	0.24	66.58
	0.2139	0.1090	0.36	81.21
	0.2130	0.1104	-0.20	78.01
	0.2143	0.1106	-0.31	76.40

Table 3. Constituent properties used in micromechanics analysis.

Property	Fiber (G40-800)	Matrix (5250-2)
E_r (ksi)	1980^a	570^d
E_z (ksi)	$41,500^b$	570^d
G_{rz} (ksi)	4930^c	213
$\nu_{r\theta}$	0.25^c	0.39^e
ν_{zr}	0.20^c	0.39^e
α_r $(10^{-6}/^oF)$	10.0^c	26.7^e
α_z $(10^{-6}/^oF)$	-0.20^c	26.7^e

[a] Computed using E_{22}=1350 ksi, square array, and constituent properties [12].

[b] [13].

[c] Estimated, see [14].

[d] [12].

[e] Estimated, see [15].

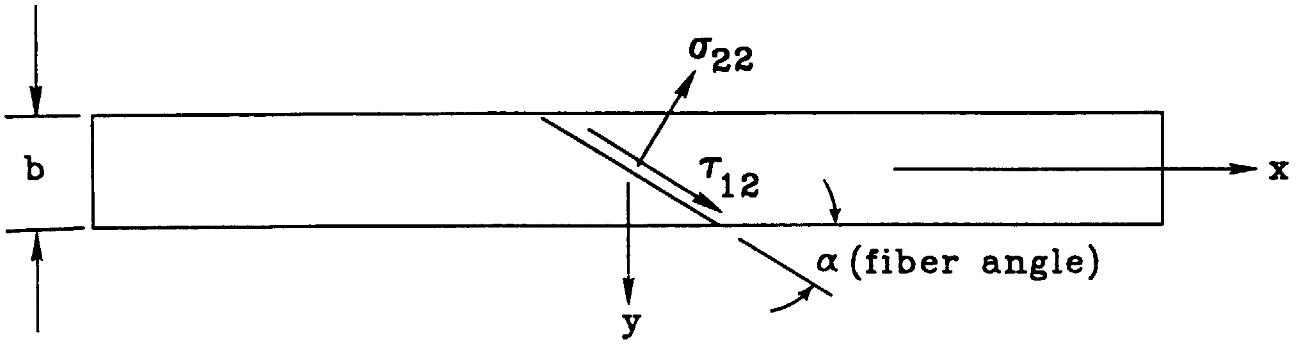

(a) Plan view of specimen.

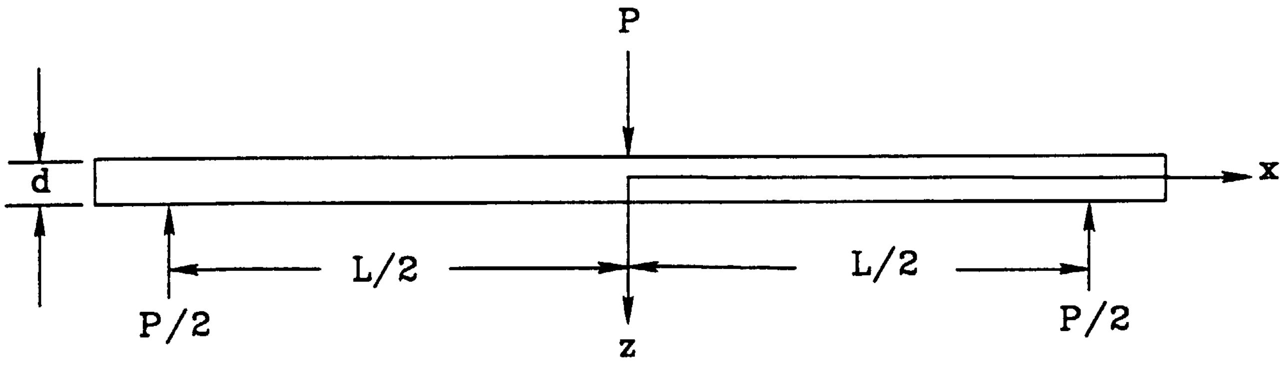

(b) Edge view of specimen with three-point loading.

Figure 1.- The off-axis flexure specimen configuration and loading.

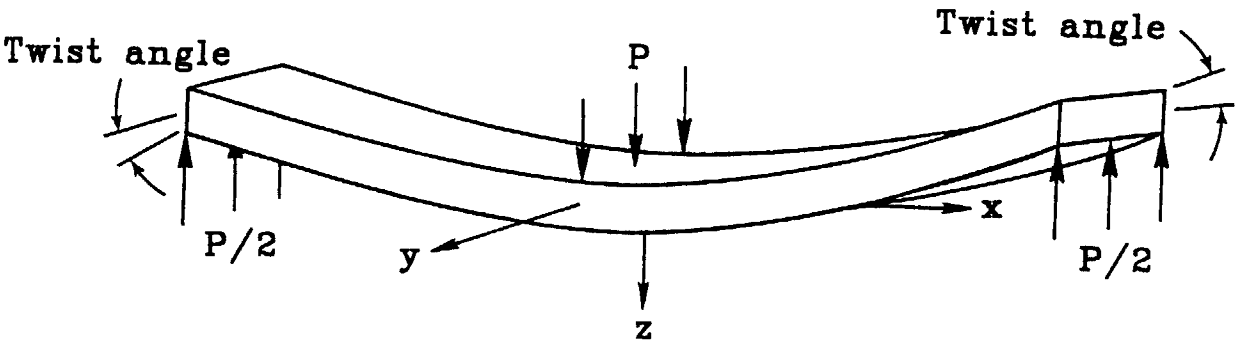

(a) Flexure and twist deformation.

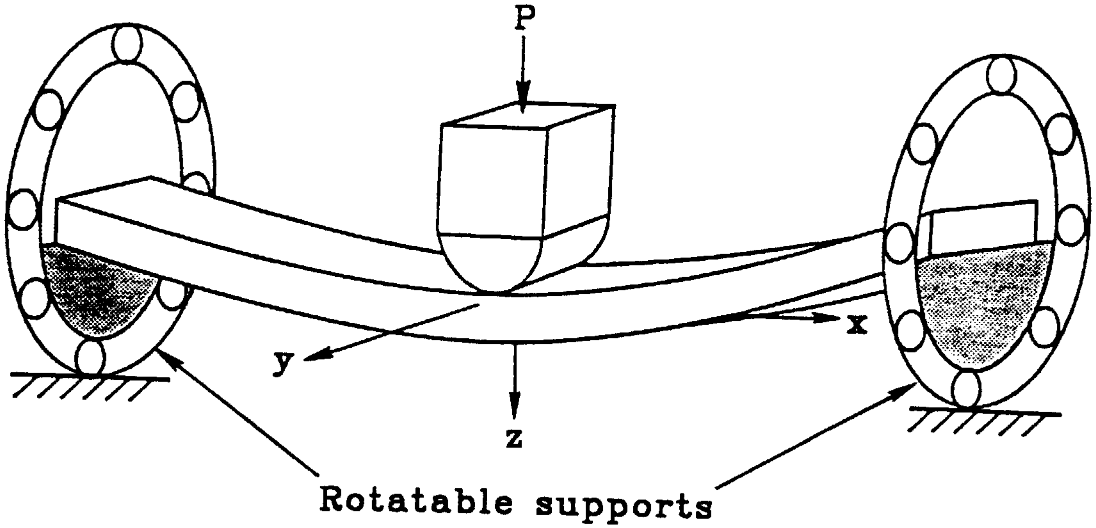

(b) Schematic of off-axis flexure test apparatus.

Figure 2.- Schematic of specimen deformation and test apparatus [5].

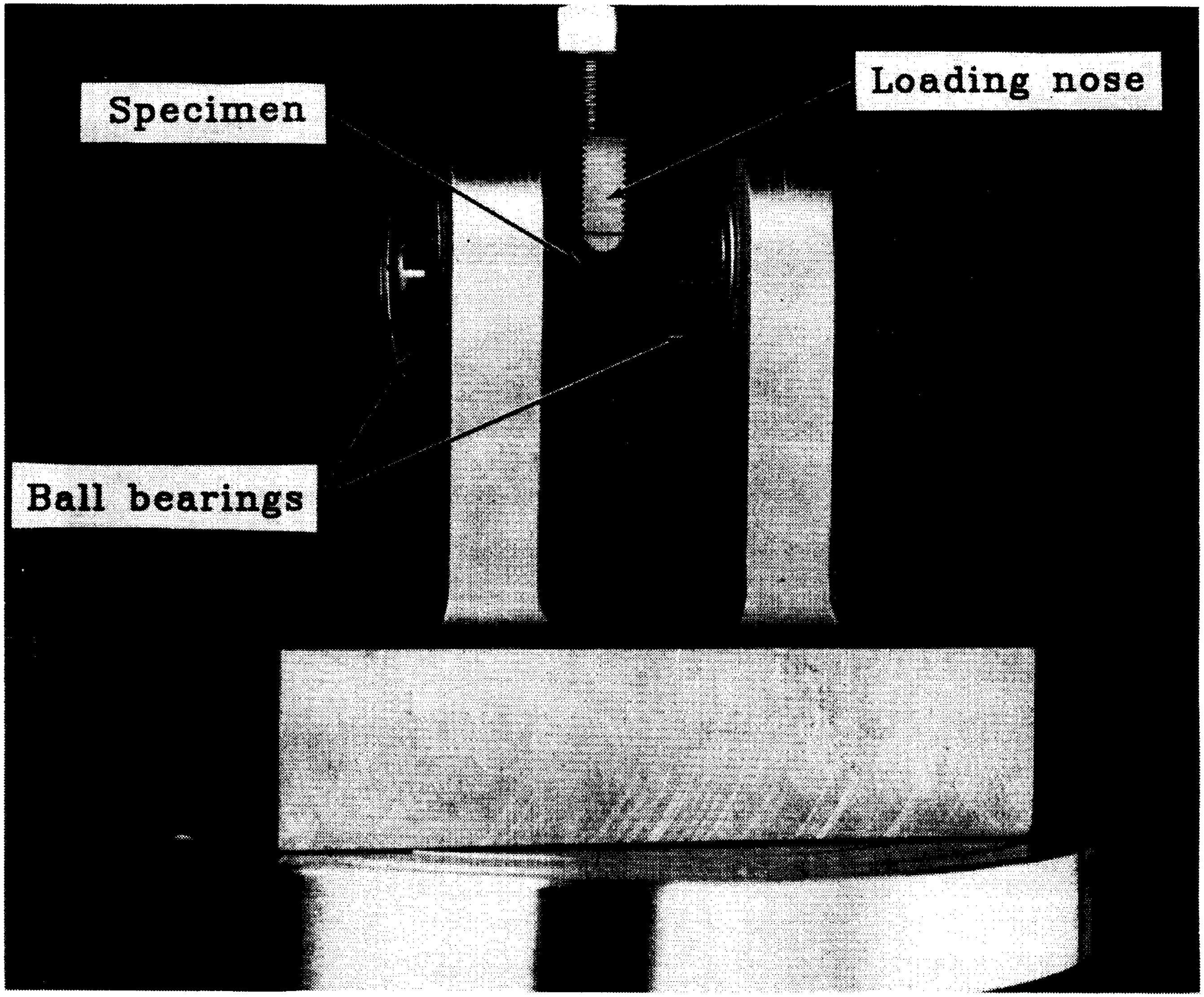

Figure 3.- Photograph of off-axis flexure test apparatus [5].

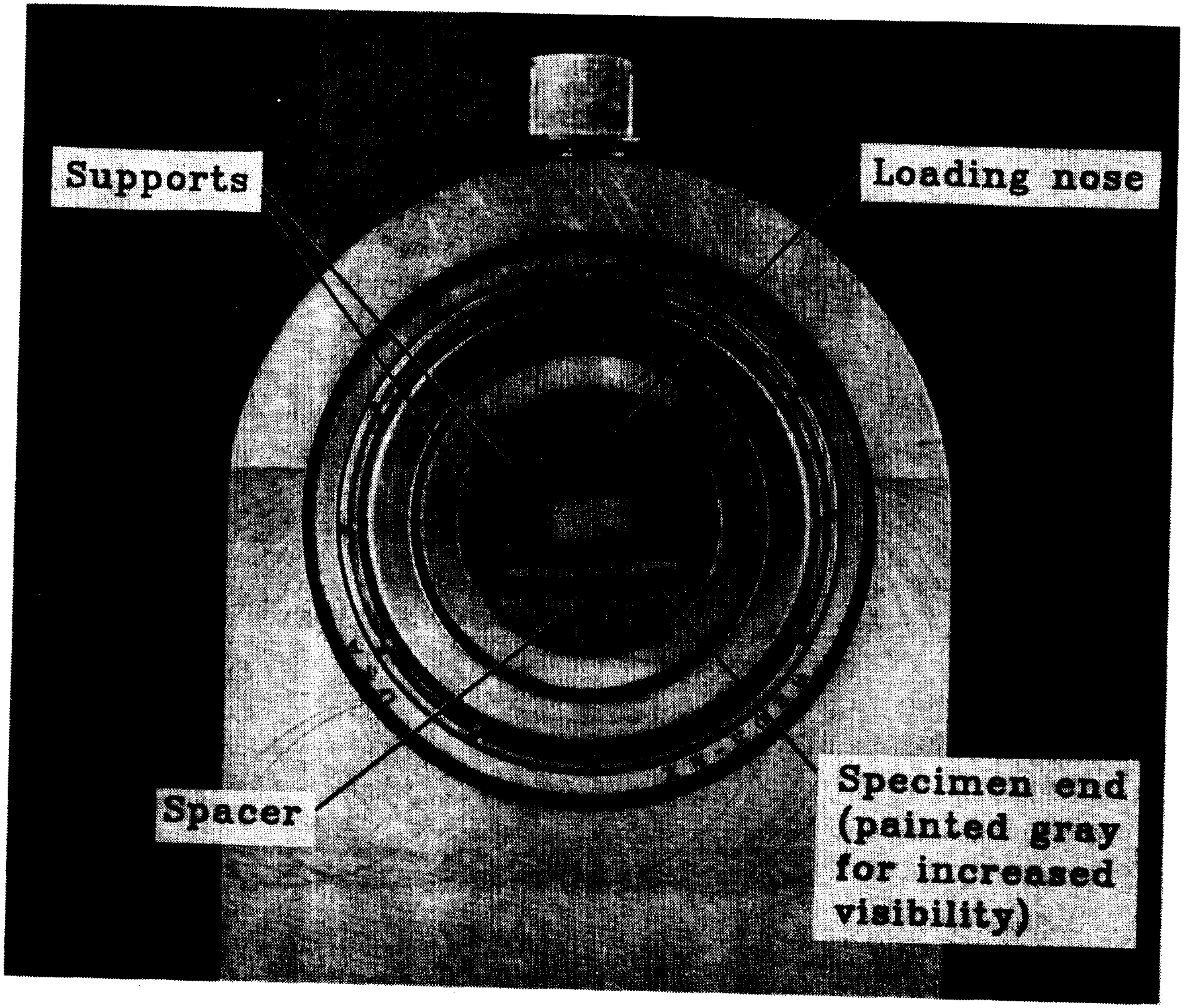

Figure 4.- End view of apparatus and deformed specimen [5].

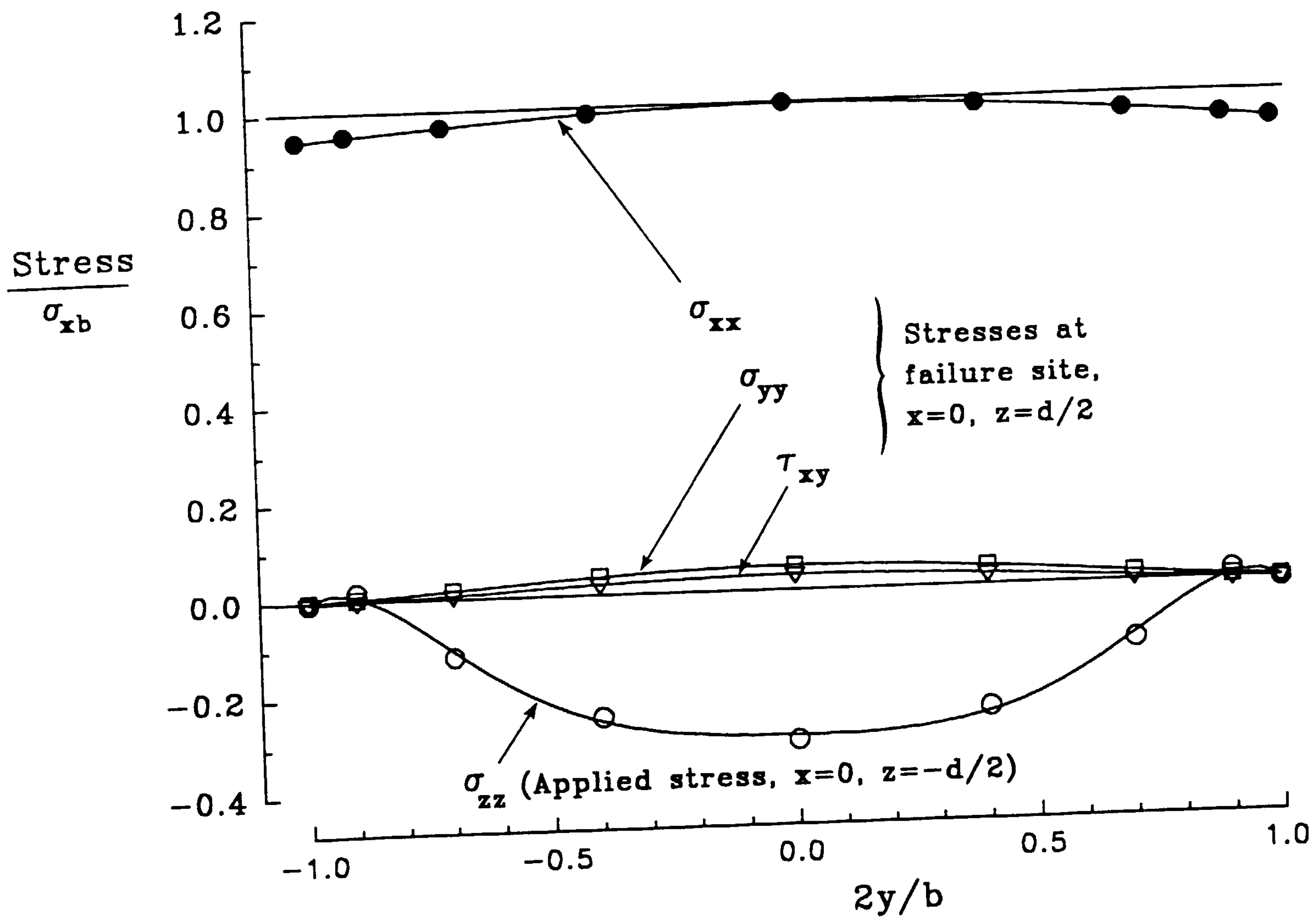

Figure 5.- Stress distributions for the $\alpha=45^{\circ}$ OAF specimen [5].

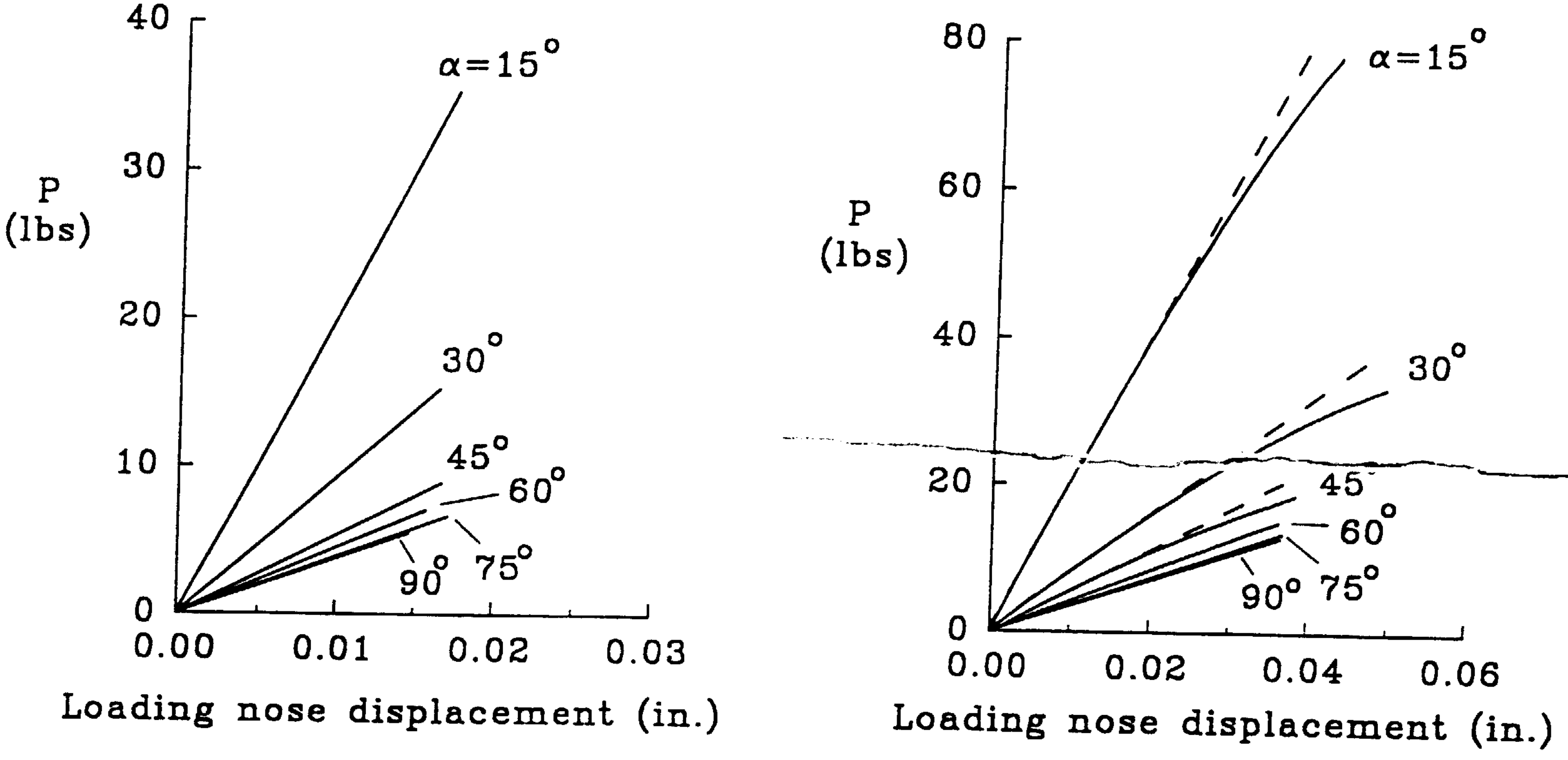

(a) Untreated laminate.

(b) Standard laminate.

Figure 6.- Typical load displacement curves to failure.

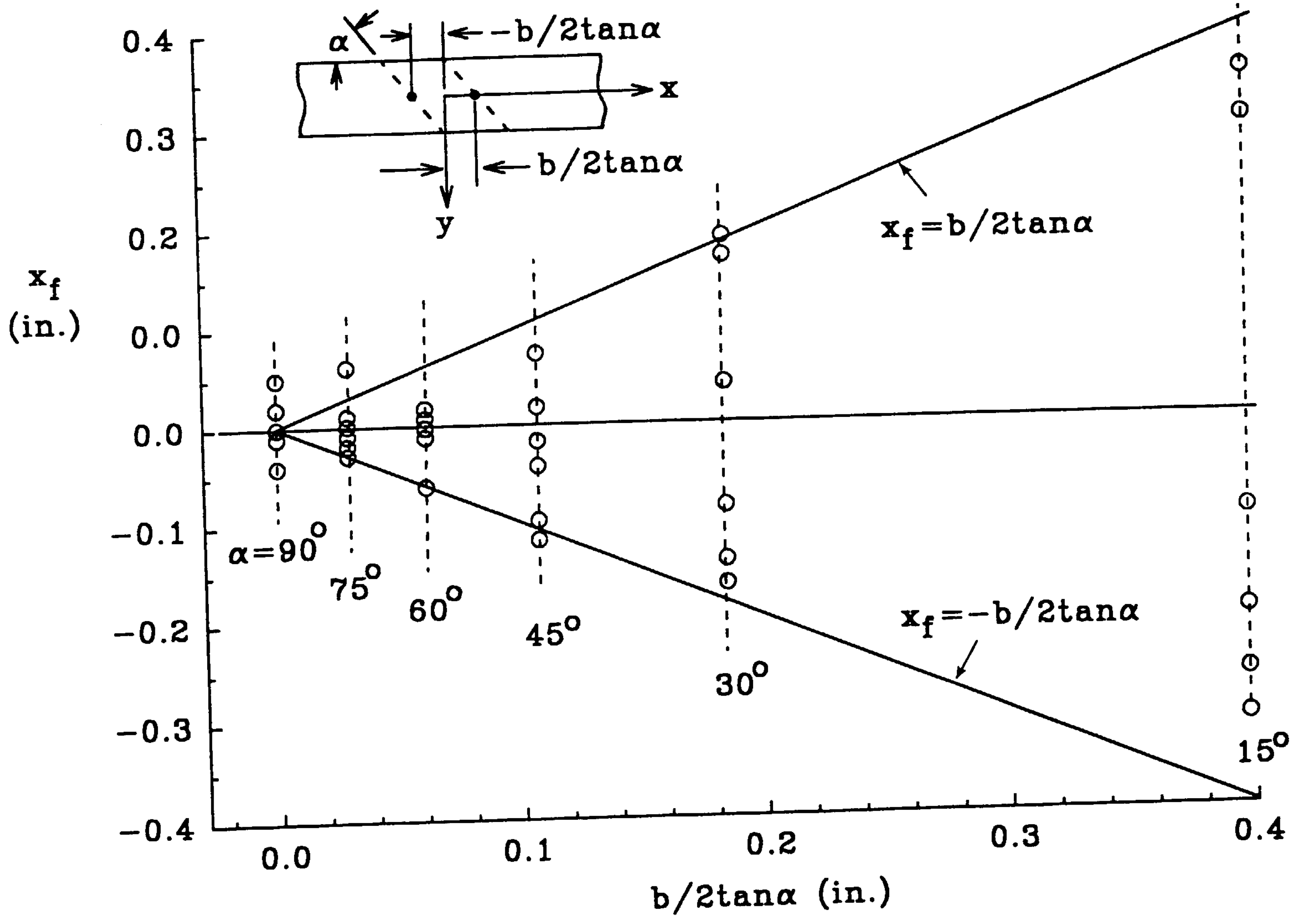

Figure 7.- Failure location data for untreated laminate.

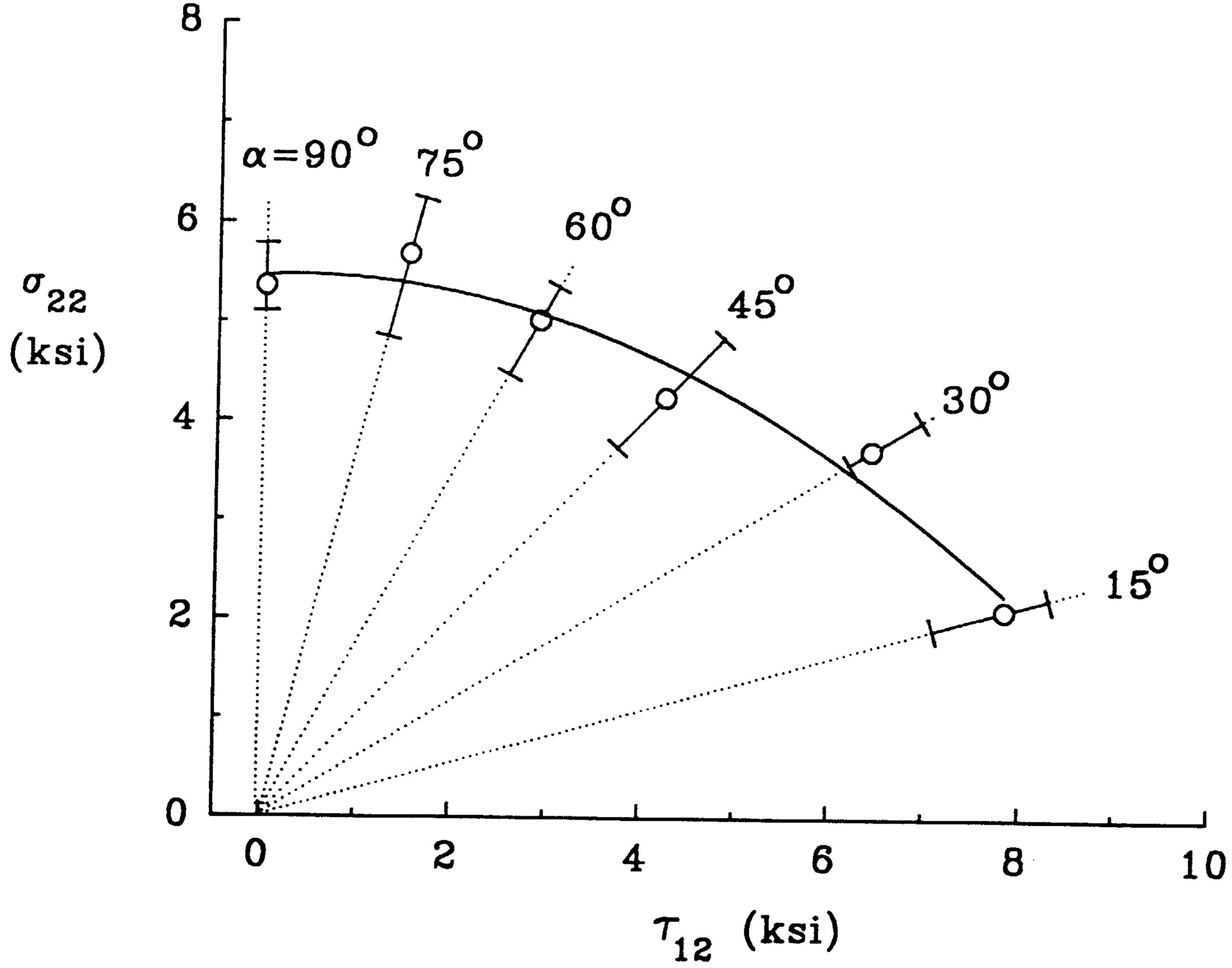

Figure 8.- Ply strength data for the untreated laminate.

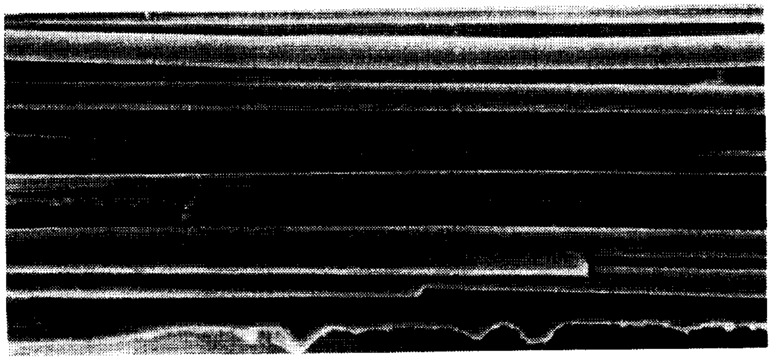

(a) $\alpha = 90^{\circ}$.

(b) $\alpha = 45^{\circ}$.

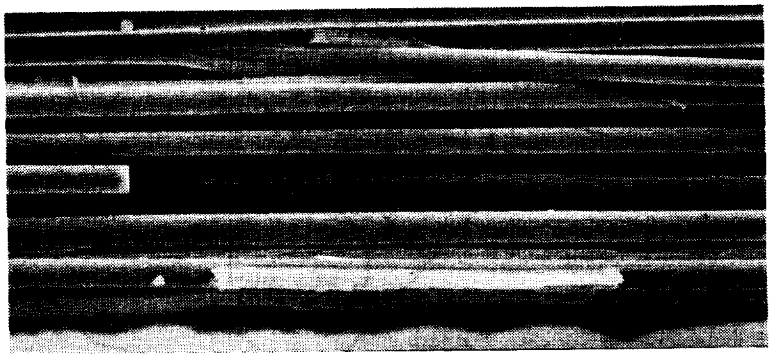

(c) $\alpha = 15^{\circ}$.

Figure 9.- Photomicrographs of fracture surfaces for the untreated laminate.

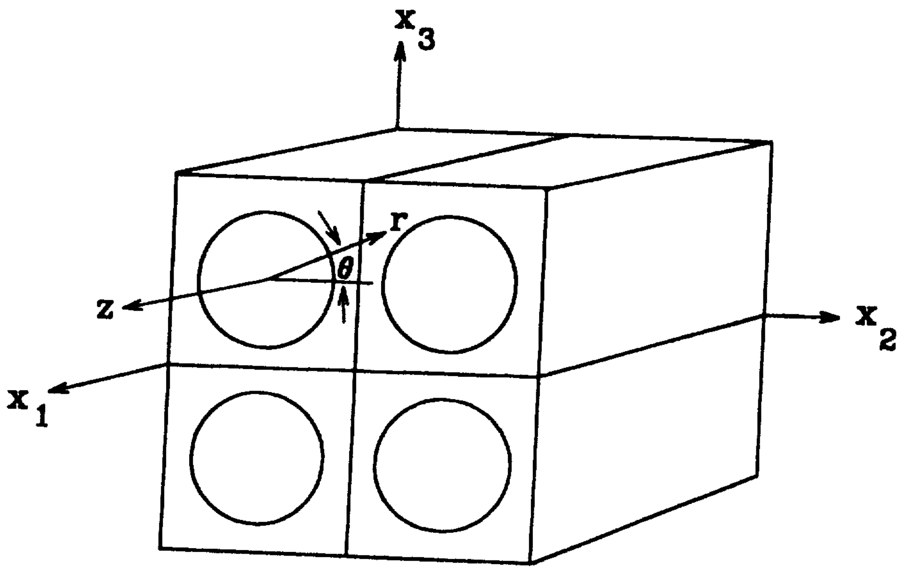

(a) Square array.

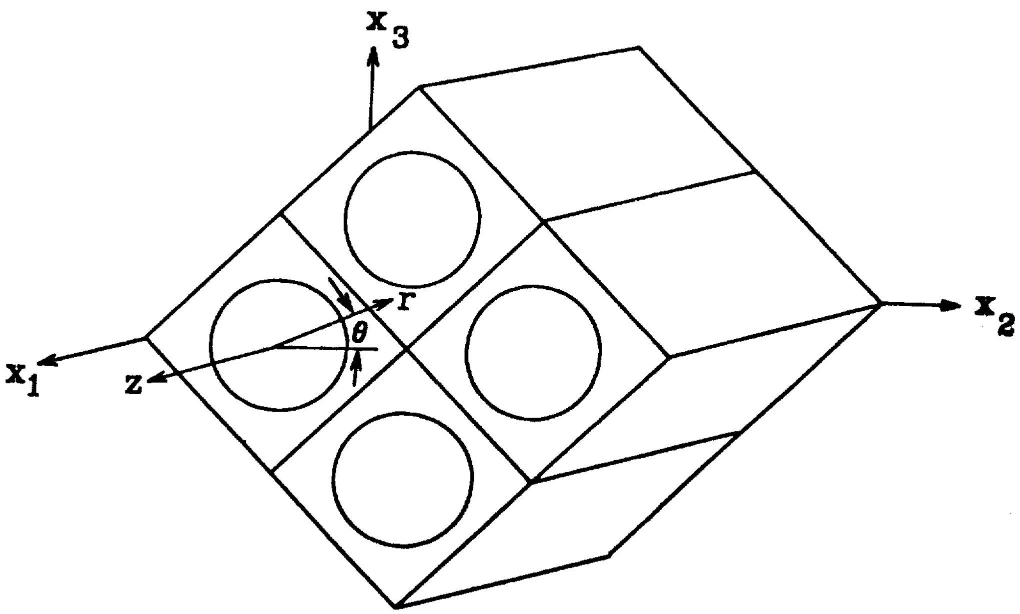

(b) Diamond array.

Figure 10.- Unit cell models for MICSTRAN micromechanics analyses.

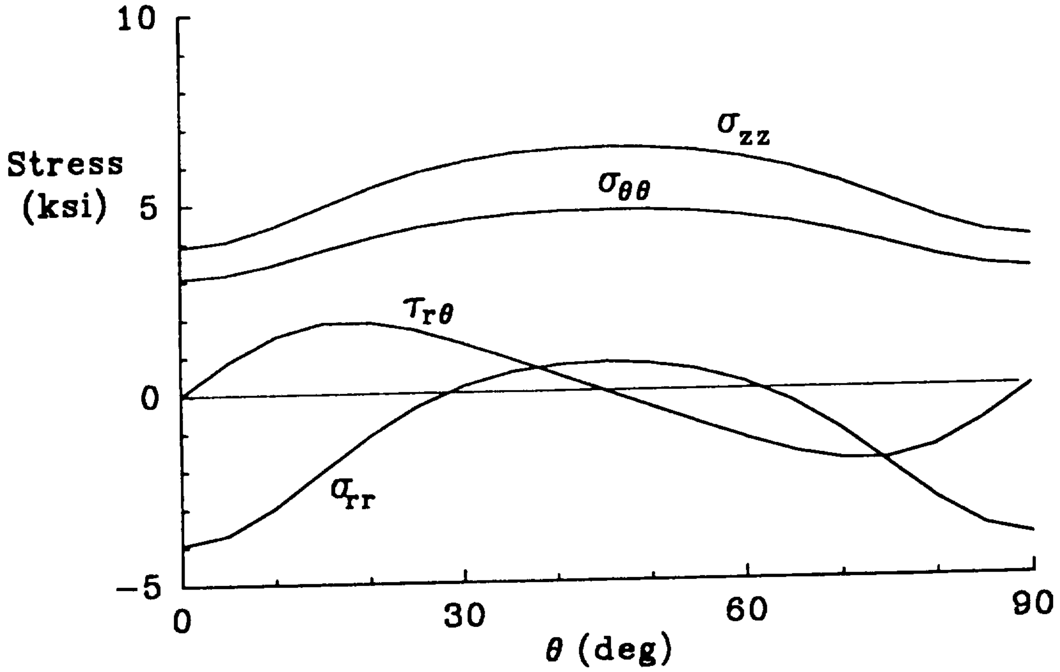

(a) Square array.

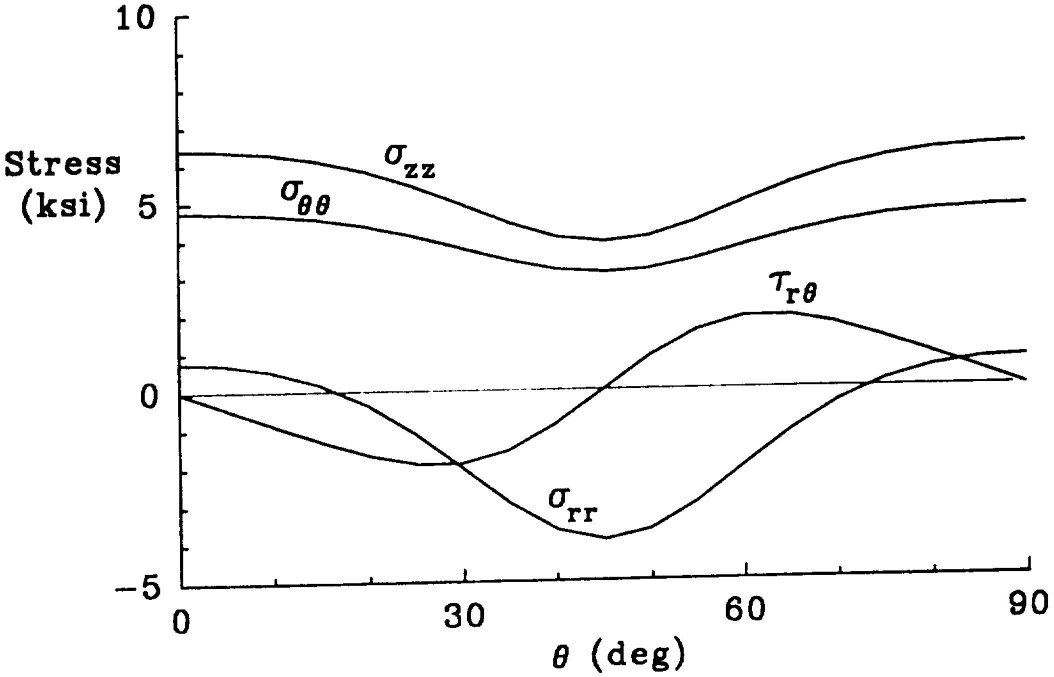

(b) Diamond array.

Figure 11.- Stress distributions along the fiber-matrix interface for thermal loading ($\Delta T = -280^{\circ}F$).

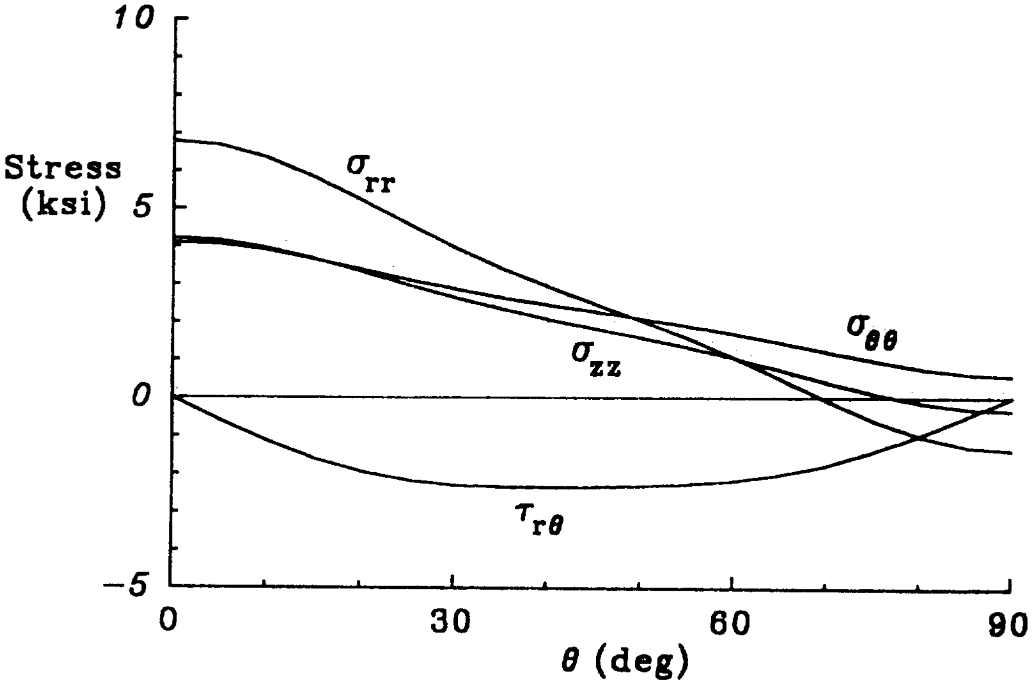

(a) Square array.

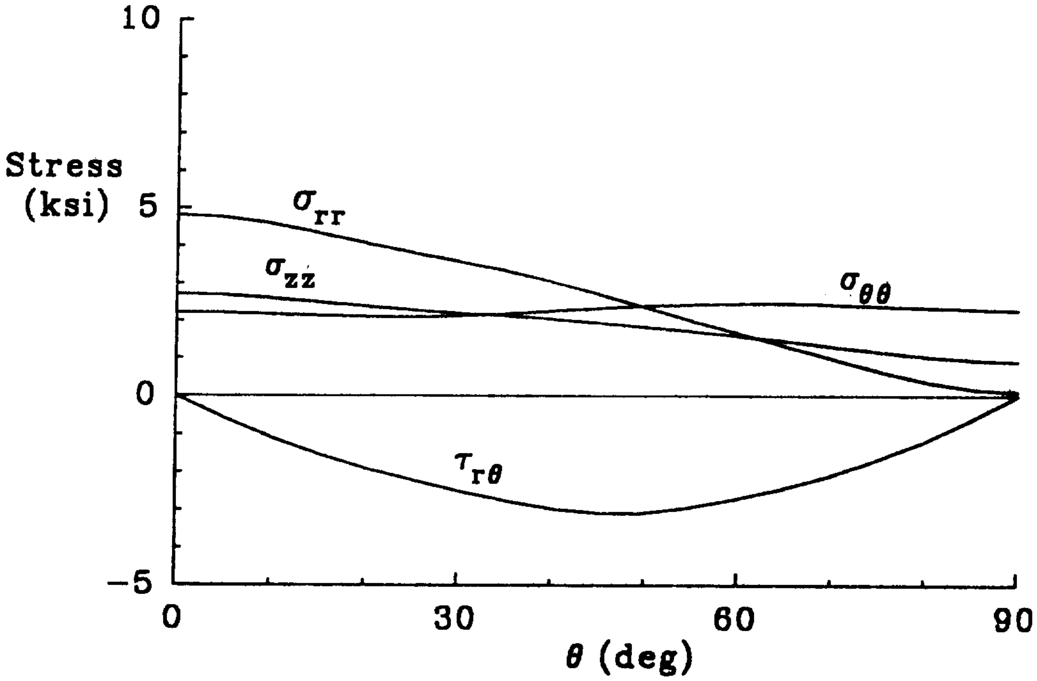

(b) Diamond array.

Figure 12.- Stress distributions along the fiber-matrix interface for transverse tensile loading (σ_{22} = 5.0 ksi).

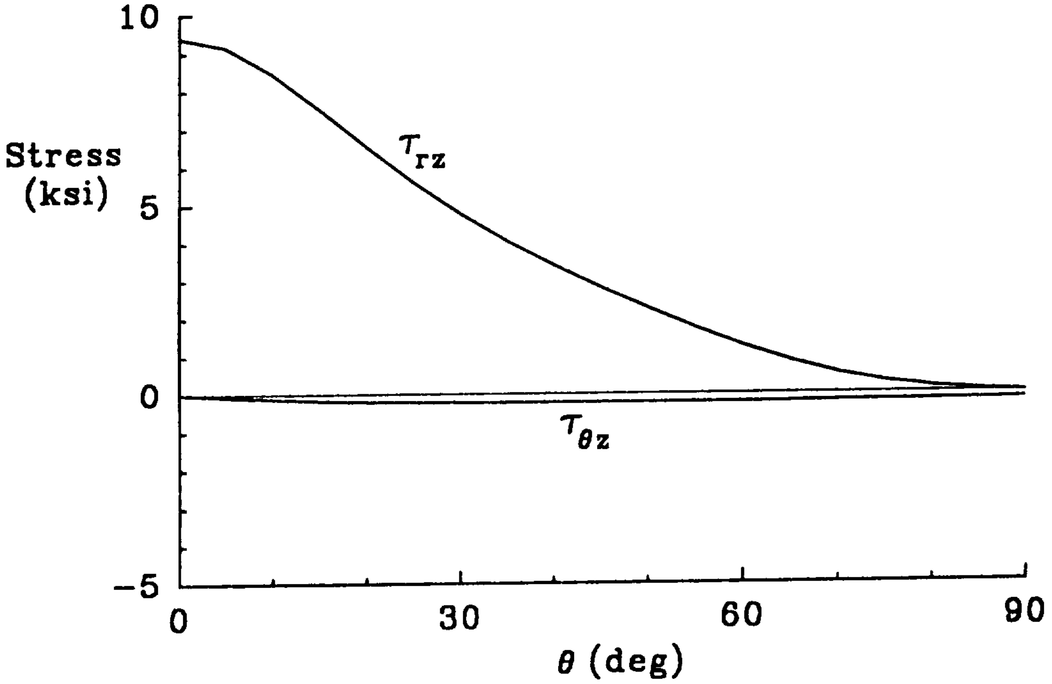

(a) Square array.

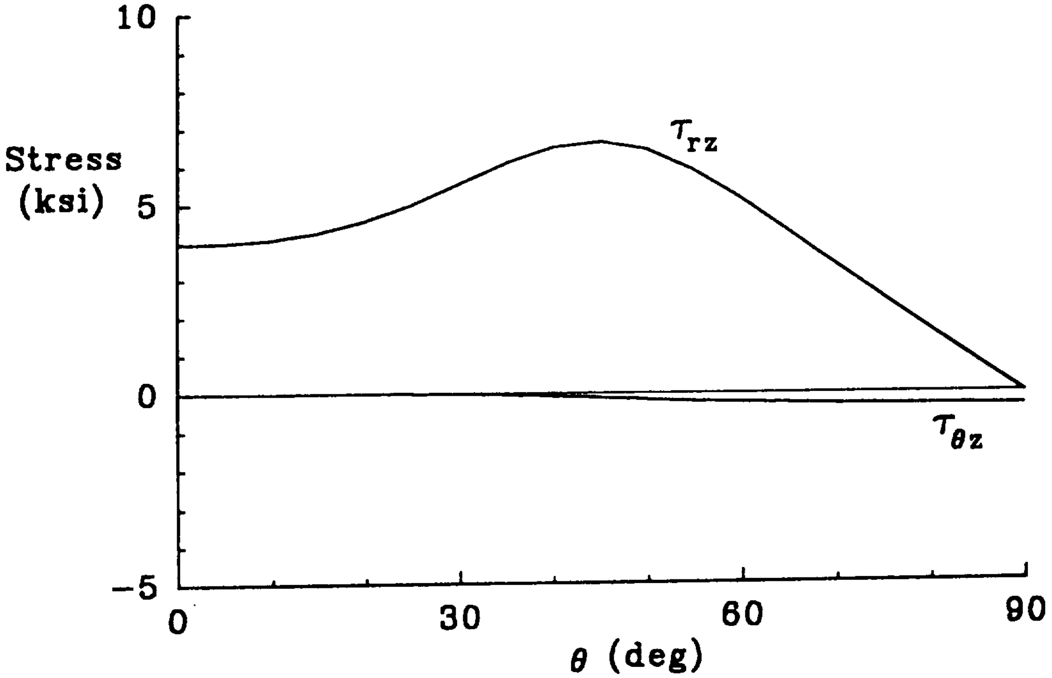

(b) Diamond array.

Figure 13.- Stress distributions along the fiber-matrix interface for longitudinal shear loading (τ_{12} = 5.0 ksi).

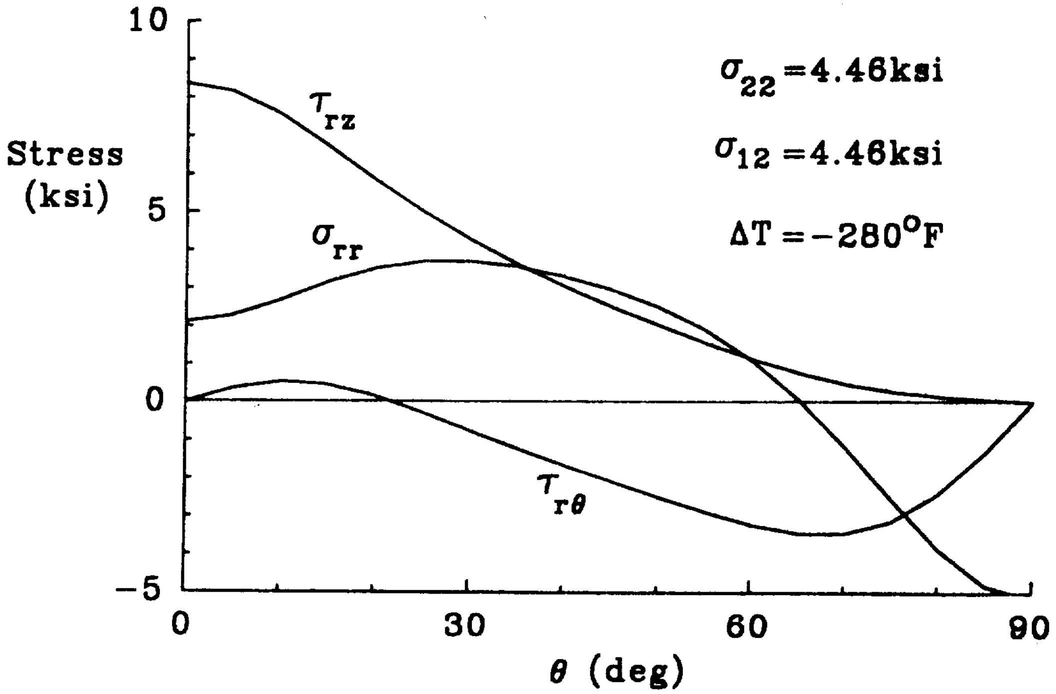

(a) Square array.

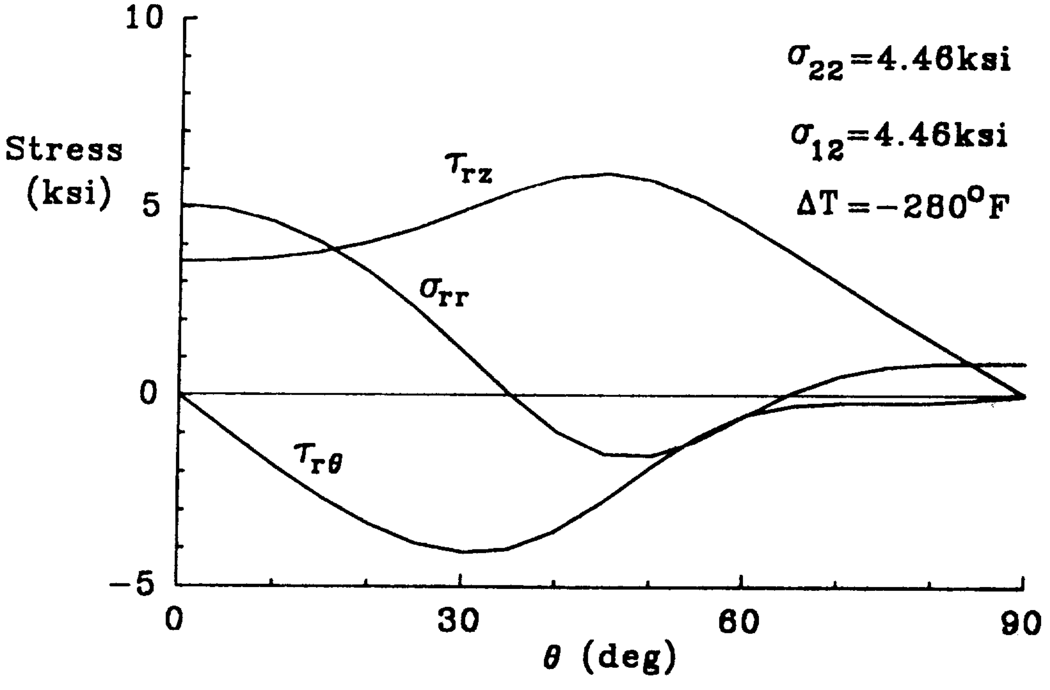

(b) Diamond array.

Figure 14.- Fiber-matrix interface stresses for the $\alpha = 45^\circ$ test case.

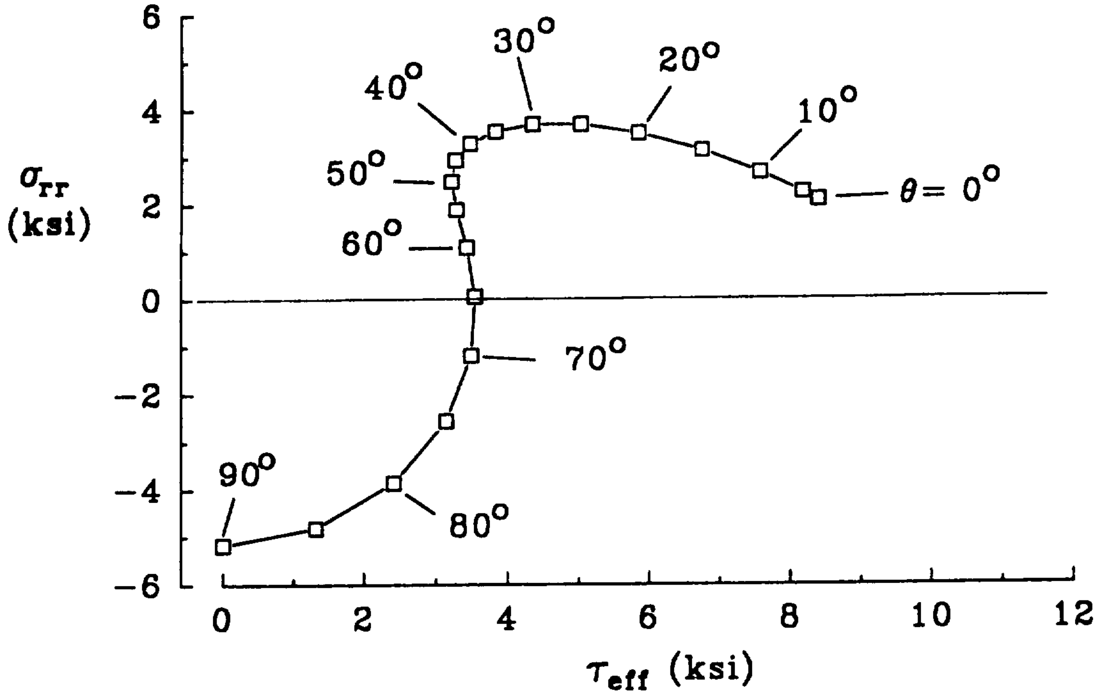

(a) Square array.

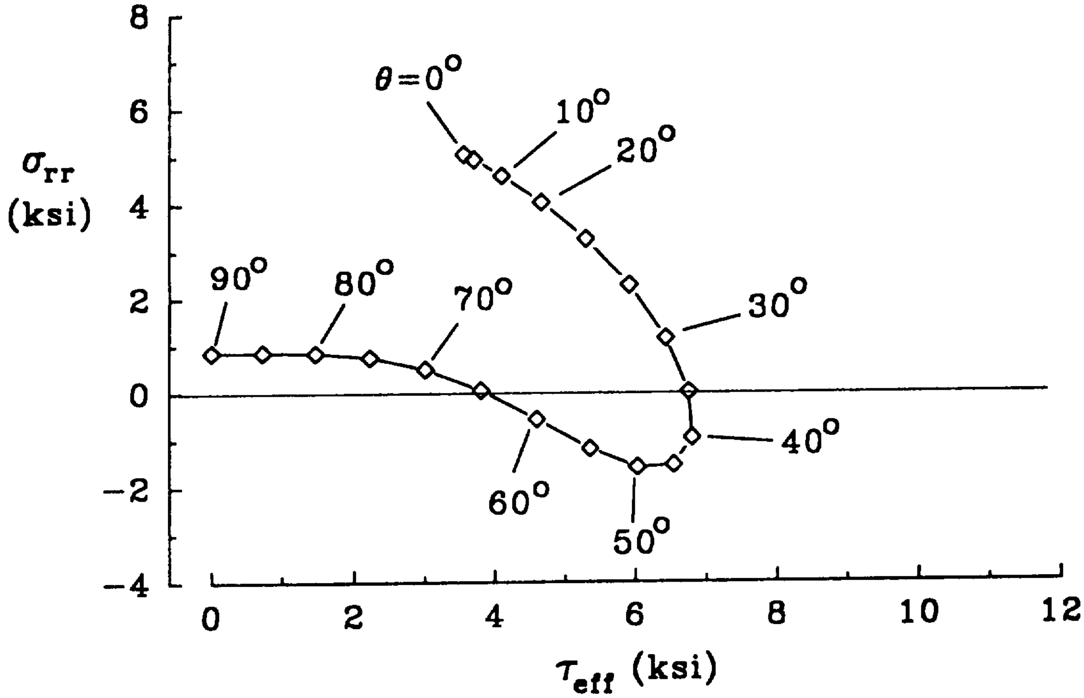

(b) Diamond array.

Figure 15.- Radial stress versus effective shear stress on the fiber-matrix interface for the α = 45° test case.

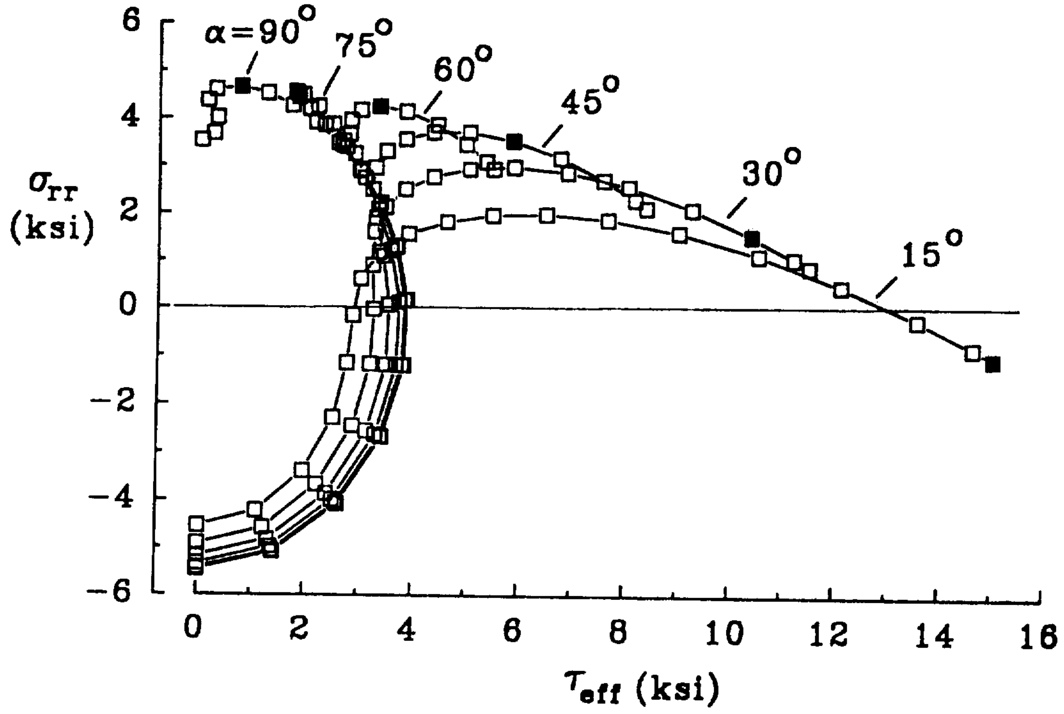

(a) Square array.

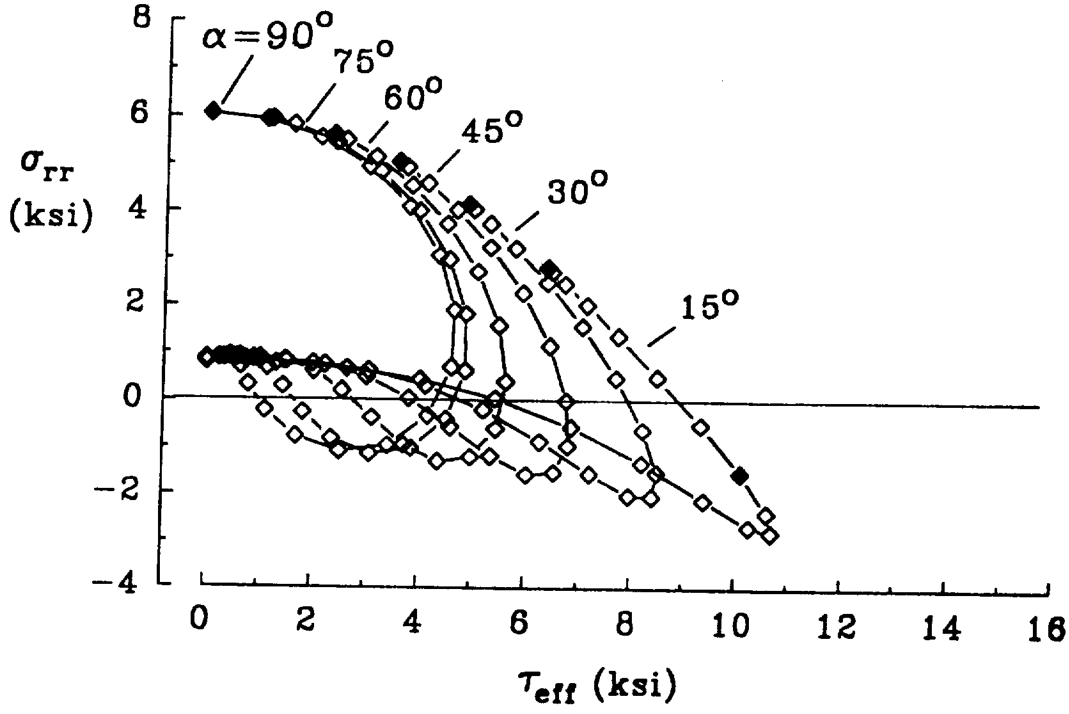

(b) Diamond array.

Figure 16.- Radial and effective shear stresses for all six test cases.

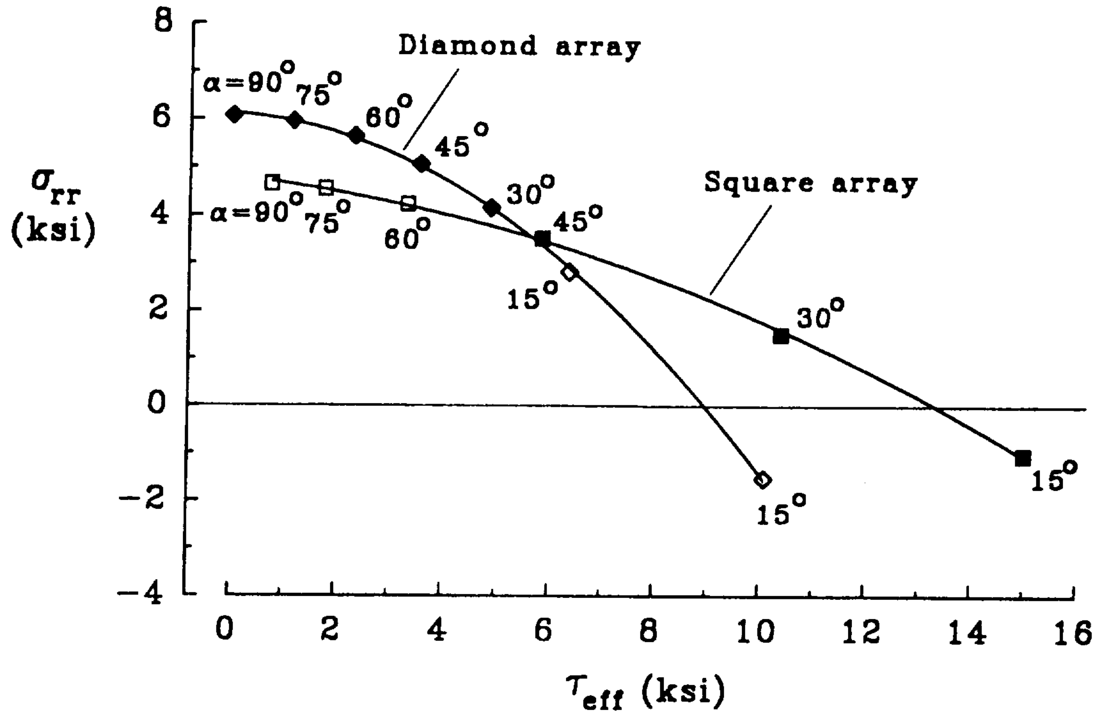

(a) Critical interface stresses for the two analysis models.

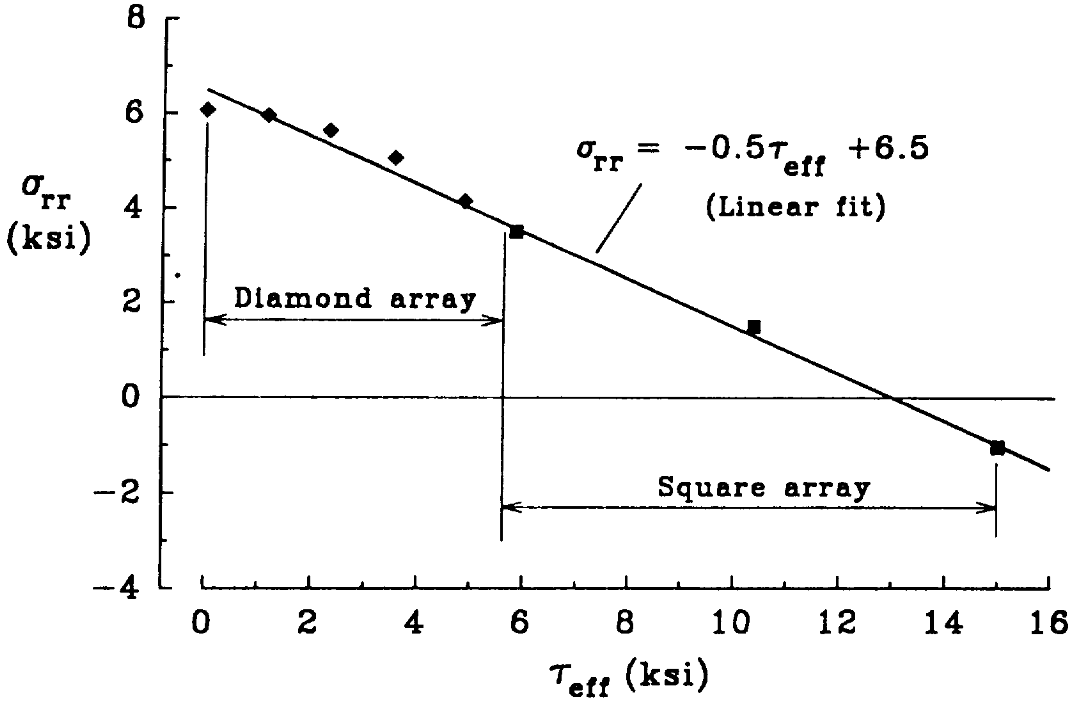

(b) Failure criterion for fiber-matrix interface.

Figure 17.- Critical interface stresses and interface failure criterion.

REPORT DOCUMENTATION PAGE

Form Approved
OMB No. 0704-0188

1. AGENCY USE ONLY *(Leave blank)*

2. REPORT DATE
July 1993

3. REPORT TYPE AND DATES COVERED
Technical Memorandum

4. TITLE AND SUBTITLE
An Analysis of Fiber-Matrix Interface Failure Stresses for a Range of Ply Stress States

5. FUNDING NUMBERS
WU 505-63-50-04

6. AUTHOR(S)
J. H. Crews, R. A. Naik, and S. J. Lubowinski

7. PERFORMING ORGANIZATION NAME(S) AND ADDRESS(ES)
NASA Langley Research Center
Hampton, VA 23681-0001

8. PERFORMING ORGANIZATION REPORT NUMBER

9. SPONSORING/MONITORING AGENCY NAME(S) AND ADDRESS(ES)
National Aeronautics and Space Administration
Langley Research Center
Hampton, VA 23681-0001

10. SPONSORING/MONITORING AGENCY REPORT NUMBER
NASA TM-108999

11. SUPPLEMENTARY NOTES
Naik: Analytical Services and Materials, Inc. , Hampton, VA
Lubowinski: Solvay Polymers, Inc., Deer Park, TX

12a. DISTRIBUTION/AVAILABILITY STATEMENT
Unclassified - Unlimited

Subject Category - 24

12b. DISTRIBUTION CODE

13. ABSTRACT *(Maximum 200 words)*

A graphite/bismaleimide laminate was prepared without the usual fiber treatment and was tested over a wide range of stress states to measure its ply cracking strength. These tests were conducted using off-axis flexure specimens and produced fiber-matrix interface failure data over a correspondingly wide range of interface stress states. The absence of fiber treatment weakened the fiber-matrix interfaces and allowed these test to be conducted at load levels that did not yield the matrix. An elastic micromechanics computer code was used to calculate the fiber-matrix interface stresses at failure. Two different fiber-array models (square and diamond) were used in these calculations to analyze the effects of fiber arrangement as well as stress state on the critical interface stresses at failure. This study showed that both fiber-array models were needed to analyze interface stresses over the range of stress states. A linear equation provided a close fit to these critical stress combinations and, thereby, provided a fiber-matrix interface failure criterion. These results suggest that prediction procedures for laminate ply cracking can be based on micromechanics stress analyses and appropriate fiber-matrix interface failure criteria. However, typical structural laminates may require elastoplastic stress analysis procedures that account for matrix yielding, especially for shear-dominated ply stress states.

14. SUBJECT TERMS
Composite; Fiber-matrix interface; Stress analysis; Ply strength; Test; Off-axis flexure

15. NUMBER OF PAGES
42

16. PRICE CODE
A03

17. SECURITY CLASSIFICATION OF REPORT
Unclassified

18. SECURITY CLASSIFICATION OF THIS PAGE
Unclassified

19. SECURITY CLASSIFICATION OF ABSTRACT

20. LIMITATION OF ABSTRACT